Optik - International Journal for Light and Electron Optics 318 (2024) 172103

Contents lists available at ScienceDirect

Optik

journal homepage: www.elsevier.com/locate/ijleo

Novel reddish-orange emitting $BaBPO_5:Eu^{3+}$ phosphor for n-UV warm white-LEDs: Synthesis and study of structural and spectroscopic investigations

T. Chandra Mohan [a,b,c,*], T. Raghu Raman [a,c], K. Venkata Rao [b,c], P. Sai Dinesh [a,b,c], Y.C. Ratnakaram [a,b,c]

[a] Department of Physics, GDC Puttur, SV University, Tirupati 517502, India
[b] Department of Physics, GDC Porumamilla, Yogi Vemana University, Kadapa 51619, India
[c] Department of Physics, Sri Venkateswara University, Tirupati 517502, India

ARTICLE INFO

Keywords:
XRD
FTIR
TG-DSC
UV–VIS DRS
Photoluminescence
Reddish-orange emission
Warm White LEDs

ABSTRACT

A novel reddish-orange emitting $2Ba_{2-x}O\text{-}B_2O_3\text{-}P_2O_5:xEu^{3+}$ (x= 0.04, 0.06, 0.08, 0.10, 0.12 and 0.14 mol%) phosphor with different concentrations of Eu^{3+} ions were synthesized through high temperature solid-state reaction technique. The crystal structure has been studied by X-ray diffraction technique for all the concentrations of Eu^{3+} ions. The morphology and elemental analysis of the optimal ~0.1 mol% concentration was examined by the SEM-EDS images. The functional groups were analysed by the FTIR characterization technique. The thermal properties were studied by the TGA-DSC analysis. The energy band gap of all the samples were analysed by using UV–VIS DRS technique. The photoluminescence properties of $BaBPO_5:Eu^{3+}$ phosphor with different concentrations of Eu^{3+} ions were investigated at λ_{em} = 611 nm and λ_{ex} = 394 nm. Variation in emission intensity with Eu^{3+} ion concentrations, phonon side bands, multi-phonon relaxation rate and energy transfer mechanisms were studied. The $BaBPO_5:Eu^{3+}$ phosphors exhibit characteristic emission peaks corresponding to $^5D_0 \rightarrow {}^7F_J$ (J = 0, 1, 2, 3, 4) transitions of Eu^{3+} ions under n-UV excitation. Among all the transitions, $^5D_0 \rightarrow {}^7F_1$ (593 nm) transition shows higher intensity and asymmetric ratio (R_{21}) for all concentrations of Eu^{3+} ions were calculated. The lifetimes of $^5D_0$ level of Eu^{3+} ions in $BaBPO_5$: Eu^{3+} phosphor were calculated by using fluorescent decay curve analysis. The CIE color coordinates reveal, reddish-orange emission in the low CCT range. These findings imply that $BaBPO_5$: $0.1Eu^{3+}$ phosphor is a promising candidate for solid-state lighting applications as well as phosphor-converted warm w-LEDs.

1. Introduction

In present technology, rare earth doped phosphors become more salient because of their high optical luminescence, long lastingness, longer lifetime, thermal stability and low energy consumption. Luminescent properties of phosphors are strongly depending on host materials [1–6]. The synthesis of phosphate phosphors, which have excellent rare earth ion solubility, low production costs, and notable emission cross-sections, has received a lot of interest. Because of their appealing qualities, which include inexpensive, easy

* Corresponding author at: Department of Physics, GDC Puttur, SV University, Tirupati 517502, India.
E-mail address: ramanphysics1985@gmail.com (T.C. Mohan).

https://doi.org/10.1016/j.ijleo.2024.172103
Received 18 March 2024; Received in revised form 18 August 2024; Accepted 28 October 2024
Available online 30 October 2024

to produce, highly resistant to chemicals, and thermally stable across a broad temperature range of 400 °C to 800 °C, phosphates are ideal host materials [7]. Along with phosphates, borate compounds also attracted the attention due to their low sintering temperature, high thermal stability and charge stability [8]. Boro phosphate-based phosphors doped with RE ions have increased the focus of the researchers due to many applications e.g., solid state display, bio labelling, plant growth lighting and fingerprint identification [9]. The addition of Ba^{2+} ions can act as a network modifier and influences the structural and optical properties of the Boro-phosphate materials [10,11]. W-LED technology is the only way for the present energy demands, which is environmentally friendly and energy saving to the next generation [12].

Currently a layer of yellow-emitting phosphors is coated to prepare commercial W-LEDs [13]. This approach has several drawbacks, such as high associated color temperatures and low color rendering indices because of inefficient red emission. Medical, engineering and house hold lightings require CRI>80. Recently high CRI W-LEDs have been developed by using n-UV LED chips (300–400 nm) using phosphors of blue, green, and red emission [14–16]. So, there is high demand for red and reddish-orange emitting phosphors which efficiently absorb in the ultraviolet region of 360–400 nm. Phosphate crystal structure rarely affects the luminescence properties of phosphates doped with trivalent rare earth ions. It was reported that very few phosphor powders are effectively absorbed near UV region and established a green and blue emission at 525 nm and 460 nm respectively [17].

Tri-valent rare earth ion doped phosphate crystals show a strong influence on their luminescence characteristics. Strong and efficient red line emitters are still a gridlock for the smart W-LEDs. In order to manufacture tricolour based WLEDs, highly effective red emitting phosphors are required. Trivalent europium (Eu^{3+}) ions are one of the most intended rare earth ions to activate phosphors and to produce red light in the visible region. Due of the 4f-4f transition, it displays sharpe and pure red emission; these transitions are quite sensitive to the host environment [18,19]. The europium has effective 4 f transitions, $^5D_0 \rightarrow {}^7F_1, {}^7F_2, {}^7F_3$ and $^7F_4$ are in the visible region, 570 nm - 720 nm. Reddish-orange or red emission can be observed from the $^5D_0 \rightarrow {}^7F_J (J=0,1,2,3,4)$ transitions with effective narrowband wing to its unique 4 f^6 configuration [20,21].

In Eu^{3+} activated phosphors, the above transitions are attributed to the magnetic and electric dipole transitions which are dominating contributors to the emissions. Normally, these Eu^{3+} doped phosphors exhibit one typical strong emission due to transition of $^5D_0 \rightarrow {}^7F_1$ or $^5D_0 \rightarrow {}^7F_2$ as the host material supports an inversion or non-inversion symmetry site [20]. In a centrosymmetric environment, the magnetic dipole $^5D_0 \rightarrow {}^7F_1$ transition of Eu^{3+} is dominating in the spectral region, 585 −600 nm with strong and sharp intensities. Electric dipole transitions, such as the hypersensitive $^5D_0 \rightarrow {}^7F_2$ transition in the spectral region 610–630 nm, which is sensitive to the complex's surroundings, are enhanced in intensity due to the distortion of the symmetry around the ion [22–24].

Phosphors doped with rare earth ions for efficient narrow band orange-red and red emission have been studied widely. Especially, the Eu^{3+} doped phosphors attracted much attention due to orange-red and red emission with NUV excitation, such as $Ca_3La_6Si_6O_{24}$: Eu^{3+} [25], $Ba_3Y_2B_6O_{15}$:Eu^{3+}[26], BaGe4O9:Eu^{3+}[27], $NaSrLa(MO_4)_3$:Eu^{3+}[28], $Ba_2La_4Y_4(SiO_4)_6O_2$: Eu^{3+} [29], $Ba_{3-x}Sr_xZnNb_2O_9$: Eu^{3+} [30], and $Ba_3CaK(PO_4)_3$: Eu^{2+} [31]. In the present investigation, another narrow band reddish-orange emitting $2Ba_{2-x}O$-B_2O_3-P_2O_5:xEu^{3+} phosphors were synthesized through the conventional solid-state technique. To the best of our knowledge, present study aims at analysing the structural, morphological, functional, thermal and optical studies of $BaBPO_5$:xEu^{3+} phosphor which shows strong reddish-orange emission in the visible region. Along with the concentration dependence of fluorescence, the colour perception and lifetime decay of $^5D_0$ level of Eu^{3+} ion is also studied. According to fluorescence properties of this phosphor, it is an excellent choice for the near UV excitation and for W-LED application.

2. Experimental procedure

2.1. Synthesis of phosphor

$2Ba_{2-x}O$-B_2O_3-P_2O_5: xEu^{3+}(x = 0.04, 0.06, 0.08, 0.1, 0.12 and 0.14 mol%) phosphors were prepared through solid state reaction technique. The chemicals utilized to make this phosphor were barium carbonate ($BaCO_3$), boric acid (H_3BO_3), ammonium di hydrogen phosphate ($NH_4H_2PO_4$), and europium oxide (Eu_2O_3). Eu_2O_3 has purity of 99.99 % and other materials are of analytical grade. In the first step the batch of 5 g were mixed in their stoichiometric ratio. The raw ingredients were fed into an agate motor and ground to a fine consistency. The batch was entirely ground to powder after homogenization, and it was first heated in a porcelain crucible for two hours at 650 °C. It was then gradually cooled to room temperature. The batch was heated to 950 °C for four hours in a porcelain crucible in the second step. Once the mixture reached room temperature, it was once more crushed into a fine powder. The batch of 5 g was weighed according to the suitable composition given below. The prepared powder can be examined by different characterisation techniques to know the suitability of the powder for rare earth doping and photoluminescence properties.

$2Ba_{0.96}O$ -B_2O_3-P_2O_5:0.04Eu^{3+}
$2Ba_{0.94}O$ -B_2O_3-P_2O_5:0.06Eu^{3+}
$2Ba_{0.92}O$ -B_2O_3-P_2O_5:0.08Eu^{3+}
$2Ba_{0.90}O$ -B_2O_3-P_2O_5:0.10Eu^{3+}
$2Ba_{0.88}O$ -B_2O_3-P_2O_5:0.12Eu^{3+}
$2Ba_{0.86}O$ -B_2O_3-P_2O_5:0.14Eu^{3+}

2.2. Characterization of the phosphor

The crystal structure and phase purity of Eu^{3+} doped ($2Ba_{2-x}O$- B_2O_3-P_2O_5:xEu^{3+}) phosphor was characterized by X-ray diffractometer (Rigaku -Smart lab (IRCC) IIT Bombay, Advance-D8 Bruker, Germany). The FTIR characterization was done with Alpha-II

Bruker spectrometer with 2 cm^{-1} spectral resolution in the wavenumber range 400–4000 cm^{-1}. Morphological studies (FESEM and EDS) were done with Thermo Fisher FEI QUANTA 250 FEG for $2BaO\text{-}B_2O_3\text{-}P_2O_5:Eu^{3+}$. Perkin Elmer LAMBDA 950 UV–VIS-NIR Spectrophotometer is used for DRS (diffuse reflectance spectra). NETZSCH STA 449 F3 Jupiter is used for TG-DSC (thermogravimetry and differential scanning calorimetry). Horiba Jobin Yvon - Fluorolog F3–111is used for photoluminescence excitation, emission and decay lifetimes of $2Ba_{2\text{-}x}O\text{-}B_2O_3.P_2O_5:xEu^{3+}$ phosphor.

3. Result and discussion

3.1. XRD analysis

The XRD profiles of $BaBPO_5$: xEu^{3+} were measured in the range 10^0-90^0 and were shown in Fig. 1. The main XRD peaks of the phosphor coincide with the crystallography open data base (COD), Entry no: 96–151–1443. Every diffraction peak's position is in good agreement, even though the doping concentrations varied and are in symmetry with those appearing in the crystallography open data base (COD). The above said information concludes the formation of pure crystalline phase of $BaBPO_5$: xEu^{3+}.

The phase analysis was done and it is observed that the $BaBPO_5$: xEu^{3+} has trigonal (hexagonal axis) crystal structure with space group P3221(#154–1) and lattice constants a=b=7.11400A^0, c=6.99300A^0, α=90^0, β=90^0, γ=120^0, V= 306.4939 $(A^0)^3$. The crystal structure of $BaBPO_5$ contains spiral tetrahedral chains built of three-membered rings. The contacts between BO_4 and PO_4 tetrahedra will produce hetero tetrahedral chain complexes (BPO_5). The boro phosphate compounds can form wide variety of crystal structures which provides a great scope for the study and exploring new functional materials, extremely for the nonlinear optical materials [32, 33].

Debye-Scherrer's formula, which is given below was used to compute the crystallite sizes [24,25]

$$D = \frac{k\lambda}{\beta\cos\theta} \tag{1}$$

where λ is the wavelength of light used, k is shape factor, β refers to the fullwidth at half maxima and θ is diffraction angle. The obtained crystallite sizes for different Eu^{3+} ion concentrations of $BaBPO_5$ phosphor are listed in the Table 1. Additionally, crystallite

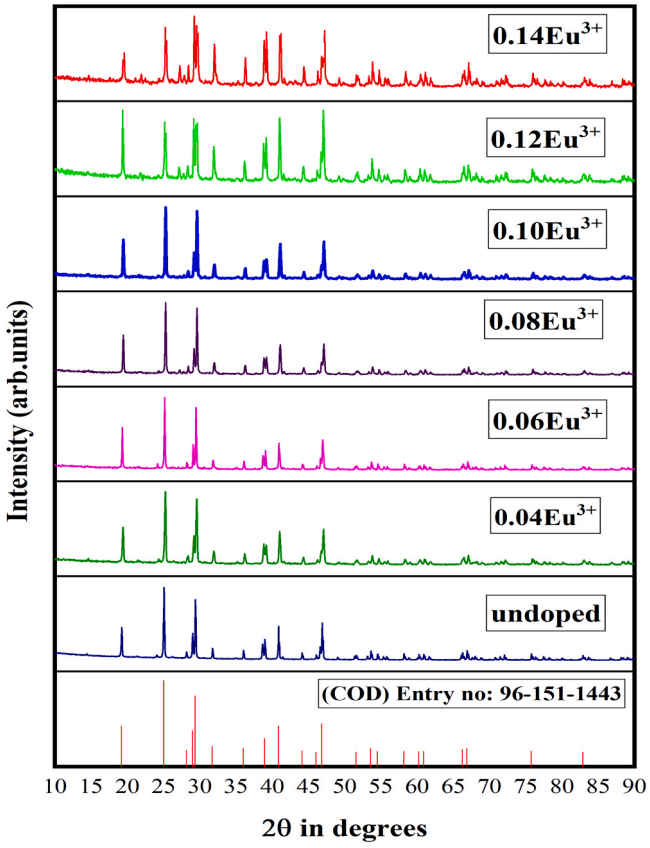

Fig. 1. Powder X-ray Diffraction profiles of $2Ba_{2\text{-}x}O\text{-}B_2O_3\text{-}P_2O_5:xEu^{3+}$ phosphor with different concentrations (x=0.04,0.6,0.08,0.10,0.12, and 0.14 mol%) of Eu^{3+}.

diameters (D) of all Eu^{3+} concentrations are calculated using William-Hall (W-H) analysis using the following equation [34], and illustrated in Table 1. Along with these, lattice strains and dislocation densities were also calculated by using W-H method [35] and depicted in Table 1.

$$\beta hkl cos\theta = \frac{k\lambda}{D} + 4\varepsilon tan\theta \quad (2)$$

where D is the crystallite size, β is fullwidth at half maxima in radians which gives the broadening of the XRD peaks, θ is the Bragg's angle in radians, ε is the lattice's micro strain, and k is the crystallite shape constant. Fig. 2 shows the graph created by plotting 4 sin θ on X-axis and β cos θ on Y-axis. The graph was linear fitted to obtain crystallite sizes (D), micro strains (ε) and dislocation densities. The calculated values for the current phosphor were depicted in Table 1 and from the values it is observed that crystallite sizes are slightly more in W-H method as compared to Debye-Scherrer method. This may be due to inclusion of micro strain in the method of W-H. It is observed that crystallite size is maximum for 0.04 mol% of Eu^{3+} and it is minimum for 0.14 mol% of Eu^{3+}. In general, the increase in dopant concentration decreases the intensity of XRD peaks, resulting in loss of crystallinity due to distortion in the lattice cell. When the Eu^{3+} ions are induced in to periodic crystal lattice of $BBPO_5$, a strain will be induced into the lattice system, resulting in crystal symmetry and periodicity of lattice [36]. As can be seen from the Fig. 1, the diffraction peaks get enlarged as the Eu^{3+} ions concentration is increased. From Table 1, it is also observed that grain size and micro strains are increasing slightly with increase in concentration of Eu^{3+} ions. This may attribute to change in crystal parameters due to doping of lesser ionic radii of Eu^{3+} ions ($1.20A^0$) in the place of higher ionic radii of Ba^{2+} ($1.35A^0$) [37].

3.2. Surface morphological analysis with EDS

The surface morphology of $BaBPO_5$: $0.1Eu^{3+}$ phosphor is examined and FESEM images are represented in Fig. 3 for 0.1 mol% Eu^{3+} doped phosphor. Particle morphologies are observed to be irregular from SEM images, and the particles also show exceptionally smooth surfaces and distinct edges. The solid-state reaction process is used to generate the present phosphor. It is condensed and formed clusters in the FESEM pictures as a result of the high temperature. The surface morphology of $BaBPO_5$: $0.1Eu^{3+}$ phosphor shows irregular shape with a particle size of several microns [20]. Fig. 4 displays the EDS spectrum and elemental mapping of $BaBPO_5$:$0.1Eu^{3+}$ phosphor, which has elements of Ba, P, O and Eu. Unfortunately, the light element boron(B) cannot find with EDS because of its low photon energy. The elemental mapping shows that the elements of Ba, P, O and Eu are homogeneous in the phosphor, indicating again that the expected phosphor of $BaBPO_5$:Eu^{3+} has been successfully prepared by solid state reaction method.

3.3. FTIR analysis

Fig. 5 represents the FTIR spectra of $BaBPO_5$: Eu^{3+} phosphors in the range 500–1300 cm^{-1}. In FTIR spectra 11 peaks were observed at 517 cm^{-1}, 545 cm^{-1},654 cm^{-1},747 cm^{-1}, 807 cm^{-1}, 855 cm^{-1}, 885 cm^{-1}, 955 cm^{-1}, 1024 cm^{-1}, 1094 cm^{-1} and 1194 cm^{-1}. All phosphate materials show bands assigned to phosphate ions $(PO_4)^{3-}$, characteristically recognised between the 450–635 cm^{-1} and 984–1200 cm^{-1} regions. The borate groups characteristically show vibrational bands in 600–870 cm^{-1} region. The PO_4 tetrahedral groups bending vibrations are responsible for the peaks at 517 cm^{-1} and 545 cm^{-1}. The bending vibrations of BO_4 tetrahedral groups are responsible for the peak at 654 cm^{-1} [38]. The peak at 747 cm^{-1} is due to bending vibrations of BO_3-O-BO_3 bonds. The peaks at 807 cm^{-1} and 855 cm^{-1} are ascribed to stretching vibrations of B-O bonds in BO_4 groups. The peak at 885 cm^{-1} is attributed to asymmetrical stretching vibrations of BO_4 and PO_4 tetrahedral groups. The peak at 955 cm^{-1} is due to asymmetrical stretching vibrations of P-O-P bonds. The peak at 1024 cm^{-1} is ascribed to asymmetrical stretching vibrations of O-P-O bond in PO_4^{3-} tetrahedrons. The peaks at 1094 cm^{-1} and 1194 cm^{-1} are due to asymmetrical stretching vibrations of PO_4 and BO_4 tetrahedral ions [33,39–41]. All the FTIR assignments of the present phosphor is represented in Table 2.

3.4. TGA-DSC analysis

TG-DSC analysis was carried out by using SDT Q600 V20.9 Build 20 in the temperature range 0 °C - 800 °C. Fig. 6 represents the concurrent TG and DTA profiles of $BaBPO_5$: Eu^{3+} phosphors.TG profile shows multistage weight loss in the phosphor attributed to multistage decomposition. The small weight loss occurred between 0 °C – 198 °C. At this stage the loss of weight is about 0.20 % and

Table 1
Crystallite sizes (D) for $2Ba_{2-x}O$-B_2O_3-P_2O_5: xEu^{3+} (x= 0.04, 0.06, 0.08, 0.10, 0.12 and 0.14 mol%) phosphor for different concentrations of Eu^{3+}.

S. NO	Concentration (x) in mol%	Debye-scherrer's method (D) in nm	William-Hall method (D) in nm	Lattice strains (ϵ) x 10^{-3}	Dislocation density (Δx) $10^{-3}(nm^{-2})$
1	0.04	69.35	82.53	1.9	0.2
2	0.06	53.53	54.80	1.5	0.3
3	0.08	38.84	41.76	3.2	0.6
4	0.1	41.85	52.52	3.1	0.5
5	0.12	41.85	52.52	3.1	0.5
6	0.14	33.05	34.32	4.0	0.9

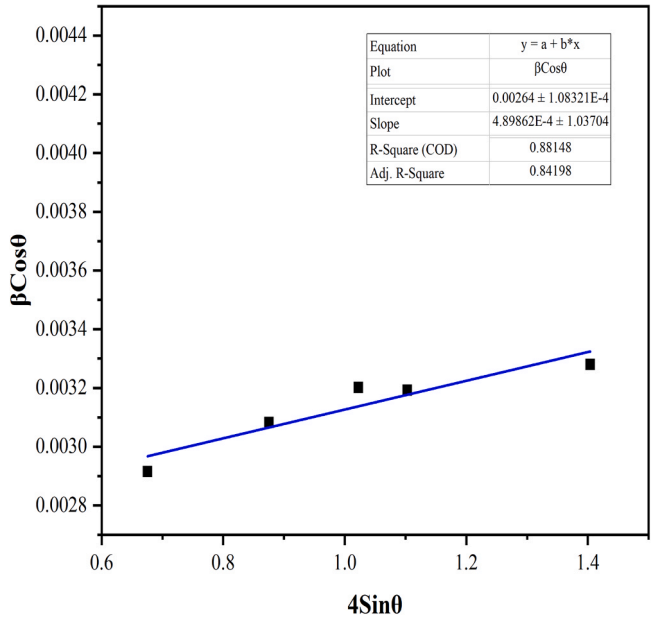

Fig. 2. W-H plot between 4 sin θ and β cos θ for 0.1 mol% of Eu^{3+} doped $BaBPO_5$ phosphor.

0.19 % in two stages, it may be due to removal of water molecules. Between 220 °C-320 °C in the second stage, there was a weight loss of 0.17 %, which may be caused by decomposition. No discernible weight loss was seen in the current phosphor between 400 °C – 800 °C, indicating that it is extremely thermally stable above 400 °C [30,42,43]. Three endothermic peaks were observed at 168 °C, 256 °C and 463 °C on the DSC curve. The first two endothermic peaks are due to removal of water and other volatile materials. The third endo thermic peak is due to glass transition of barium boro-phosphate [43,44].

3.5. *Diffuse reflectance spectra (DRS) analysis*

The diffuse reflectance spectra (DRS) of $BaBPO_5$:xEu^{3+} phosphor for different concentrations of Eu^{3+} ions are present in Fig. 7 and in the range, 200 nm – 2300 nm. The figure indicates that the charge transfer transition is responsible for the big bump at ≈ 241 nm, which is caused by host absorption. The weak transition at ≈391 nm (350 nm - 500 nm) is due to 4f-4f transitions of Eu^{3+} ions [30].

Tauc (1996) suggested an optical absorption spectra-based approach for determining the band gap energy. This Tauc method is based on assumption that the energy – dependent absorption coefficient 'α' can be expressed by the following Eq. (3) [45]:

$$(\alpha h\upsilon)^{1/\gamma} = B\,(h\upsilon - E_g) \tag{3}$$

where υ is the photon's frequency, B is a constant, h is the Plank's constant, and E_g is the band gap energy. Depending on the kind of electron transition, the γ factor is equal to ½ for direct transitions and 2 for indirect transition band gaps. The diffuse reflectance spectra is typically used to calculate the band gap energy. Kubelka and Munk's theory states that the Kubelka-Munk function ($F(R_\infty)$) can be used to convert the measured reflectance spectra to the corresponding absorption spectra by applying equation given below [45].

$$F(R\infty) = \frac{K}{S} = \frac{(1-R_\infty)^2}{2R_\infty} \tag{4}$$

where K and S stands for the absorption and scattering coefficients respectively and $R_\infty = R_{sample}/R_{standard}$ represents the reflectance of an infinitely thick specimen. Instead of α if we substitute $F(R_\infty)$ into equation.3, then it gets the form (5)

$$(F(R_\infty) \bullet h\upsilon)^{1/\gamma} = B\,(h\upsilon - E_g) \tag{5}$$

Using Kubelka-Munk function and DRS spectral data, the optical energy band gaps of $BaBPO_5$:xEu^{3+} (x=0.04, 0.06, 0.08, 0.1, 0.12 and 0.14 mol%) phosphor were determined. The aforementioned relation (Eq. 5) was used to convert the DRS data into absorption spectra. To find direct energy band gap, graphs were plotted between 'h υ' and $[F(R_\infty)\ h\upsilon]^2$ by taking data on X-axis and Y-axis respectively. At the point of inflection, a tangent line is constructed, and the plot's X-axis intersection point provides an estimate of the band gap energy. From the graph, the band gap energy values of $BaBPO_5$:xEu^{3+} phosphor are 4.60, 4.57, 4.56, 4.57, 4.58 and 4.54 for 0.04, 0.06, 0.08, 0.10, 0.12 and 0.14 mol% concentrations of Eu^{3+} respectively. The data shows that the band gap energy values are slightly varying from 0.04 mol% Eu^{3+} to 0.14 mol% Eu^{3+} ions.

To find indirect energy band gap, graphs were plotted between 'hυ' and $[F(R_\infty)\ h\upsilon]^{1/2}$ by taking data on X-axis and Y-axis respectively. The X-axis intercept point of the tangent line drawn to Tauc plot gives the band gap energy. The measured band gap

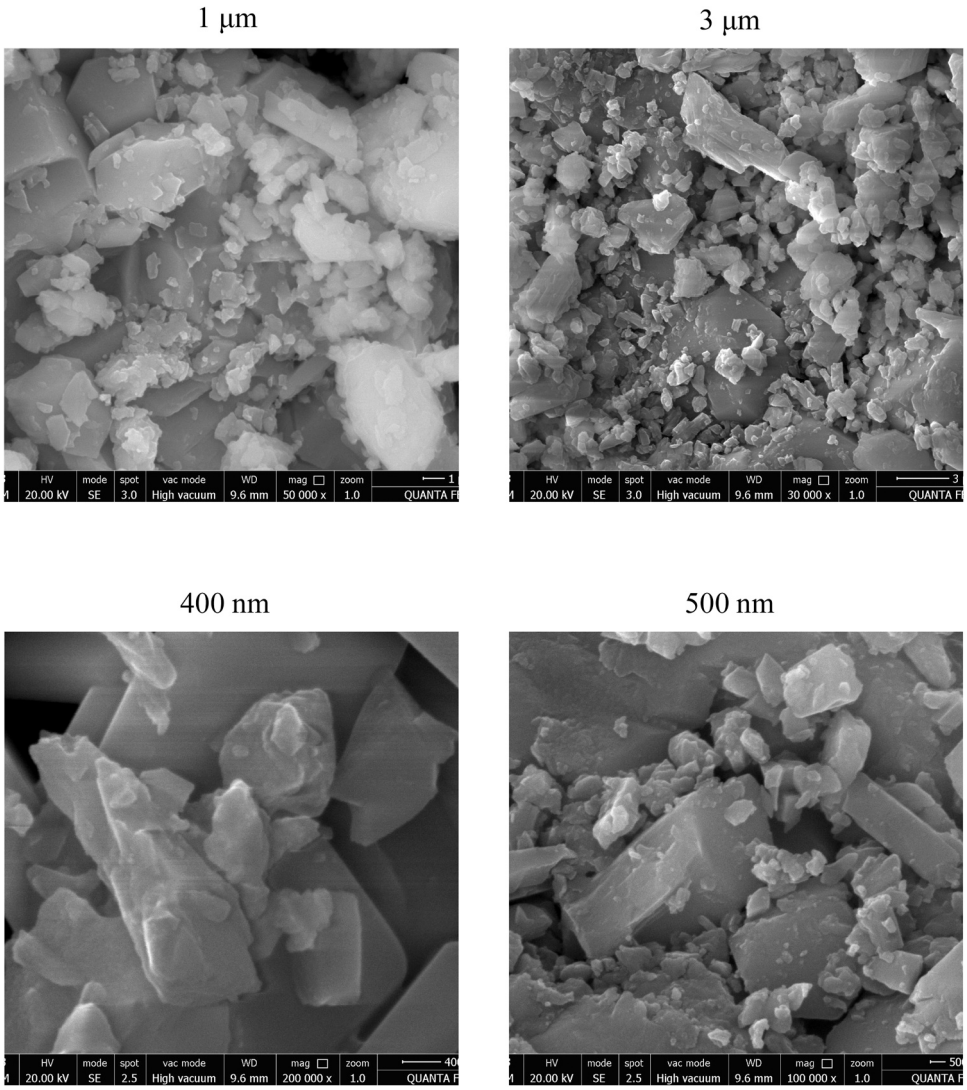

Fig. 3. Scanning electron microscopy images of $BaBPO_5$: 0.1 % Eu^{3+} phosphor with different magnitudes.

values from the graphs are 4.06, 4.03, 3.90, 4.04, 3.97, and 4.01 for 0.04, 0.06, 0.08, 0.10, 0.12 and 0.14 mol% of Eu^{3+} respectively. The band gap energy values are nearly same for 0.04 mol% Eu^{3+} to 0.14 mol% Eu^{3+} ions. The higher band gap values states that it is a suitable host in phosphate family. The wide band gap energy values play a vital role in many optoelectronic devices at higher voltage applications [46]. It is evident from the given results that when the dopant concentration rises, the band gap values gradually decrease. The variation in band gap energies is due to introduction of RE ions into host lattice which introduce intermediate energy levels of impurity bands in the host lattice. The increase in concentration of RE ions changes the crystallite size which in turn decreases energy band gaps. Further variations in energy band gap may be due to crystalline imperfections and compositional inhomogeneity [46]. The current phosphor is appropriate for photovoltaic applications since its energy band gap values change little with dopant concentrations.

3.6. Luminescence properties

3.6.1. Excitation spectra and phonon side band analysis

Fig. 8 displayed the photoluminescence excitation spectrum of the $BaBPO_5$: $0.1Eu^{3+}$ phosphor. The 4f-intra transitions in the Eu^{3+} ions are responsible for the excitation apexes, which are located between 250nm and 550nm. The excitation spectrum was observed at characteristic emission wavelength i.e., 611 nm. The observed excitation peaks are at 298 nm ($^7F_0 \rightarrow {}^5I_5$), 318 nm ($^7F_0 \rightarrow {}^5H_6$), 361 nm ($^7F_0 \rightarrow {}^5D_4$), 382 nm ($^7F_0 \rightarrow {}^5G_2$), 394 nm ($^7F_0 \rightarrow {}^5L_6$), 414 nm ($^7F_0 \rightarrow {}^5D_3$), 464 nm ($^7F_0 \rightarrow {}^5D_2$), and 525 nm ($^7F_0 \rightarrow {}^5D1$). Among all the peaks, higher intensity peak is observed at 394 nm. This excitation wavelength is far away from mercury (Hg) excitation and this is the main characteristic wavelength range (350–395 nm) in solid-state lightning. This phosphor can be efficiently excited by near UV light,

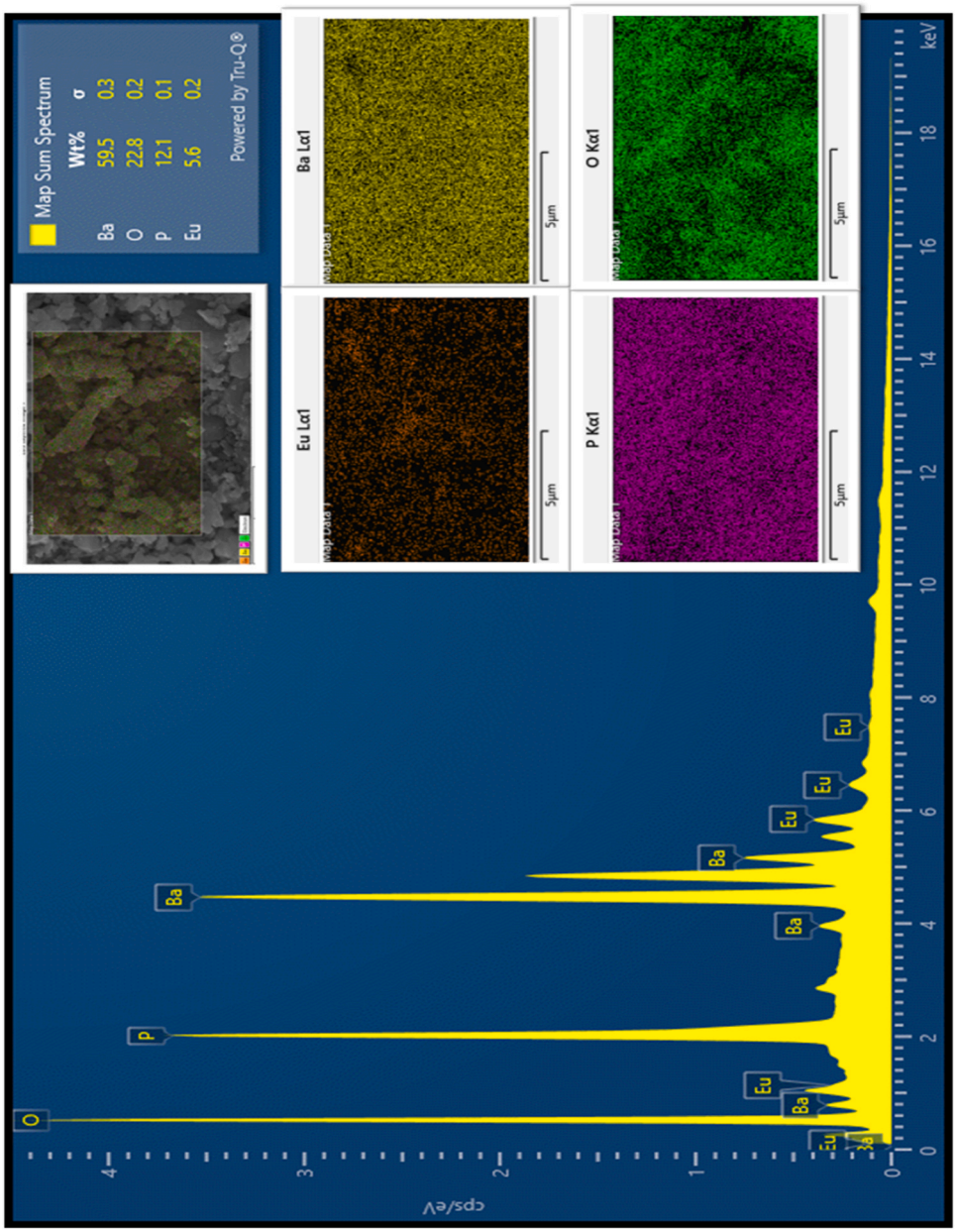

Fig. 4. EDS spectrum and elemental mapping analysis of $BaBPO_5$:0.1 %Eu^{3+} phosphor.

as demonstrated by the excitation and this is just what UV chip pumped multi-phosphor converted white LEDs [46–50].

To look into local environment around Eu^{3+} ion and phonon energy, we examine the phonon side bands associated with $^7F_0 \rightarrow {}^5D_2$ pure electronic transition (PET) [30]. Fig. 9 shows the phonon side band spectrum of present phosphor. Among all the transitions of 4f-4f of Eu^{3+} ions, the $^7F_0 \rightarrow {}^5D_2$ transition is usually considered to find the phonon side bands because the energy difference between $^5D_2$ to $^5D_3$ is large (2500 cm^{-1}) and there are no energy levels between these two levels. Two smaller side bands are observed on the higher energy side of pure electronic band (PEB) in the Fig. 9. These bands are called as phonon side bands. The PEB is called as zero phonon line (ZPL) and it is in the range 21367–21691 cm^{-1}. In the present phosphor, two PSBs were observed at 22222 cm^{-1} and 22522 cm^{-1}. The PSBs were amplified by factor 100 for the visibility. The phonon energies ($\hbar\omega$), electron-phonon coupling strengths (g) and multi phonon relaxation rates (W_{MPR}) of RE^{3+} ion in present phosphor is calculated and estimated with the help of phonon side band spectrum. The phonon energy can be approximated by the energy difference between PEB (pure electronic band) and PSB (phonon side band) around the Eu^{3+} ions [51].

The phonon energies ($\hbar\omega$) of the present phosphor were observed as ~673 cm^{-1} and 972 cm^{-1} and these phonon energies are very close to vibrational modes in the IR spectrum of present phosphor i.e., ~654 cm^{-1} and ~ 955 cm^{-1}. The electron-phonon coupling

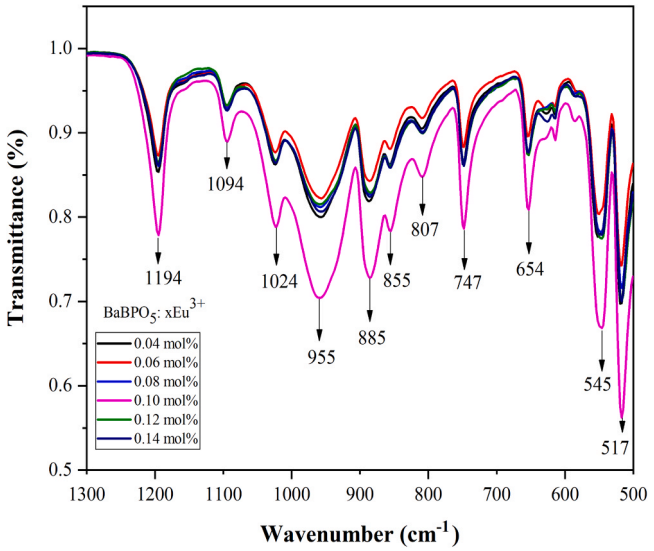

Fig. 5. FTIR spectra of $BaBPO_5$:0.1 %Eu^{3+} phosphor.

Table 2
FTIR assignments of $BaBPO_5$:Eu^{3+} phosphor for different concentrations of Eu^{3+} ions.

S.NO	Wave number(cm^{-1})	FTIR assignments
1	517,545	Bending vibrations of PO_4 tetrahedral groups
2	654	Bending vibrations of BO_4 tetrahedral groups
3	747	Bending vibrations of BO_3-O-BO_3 bonds
4	807,855	Stretching vibrations of B-O bond in BO_4 groups
5	885	Asymmetrical stretching vibrations of BO_4 and PO_4 tetrahedral groups
6	955	Asymmetrical stretching vibrations of P-O-P bonds
7	1024	Asymmetrical stretching vibrations of O-P-O bond in PO_4^{3-} tetrahedrons
8	1094,1194	Asymmetrical stretching vibrations of PO_4 and BO_4 tetrahedral ions

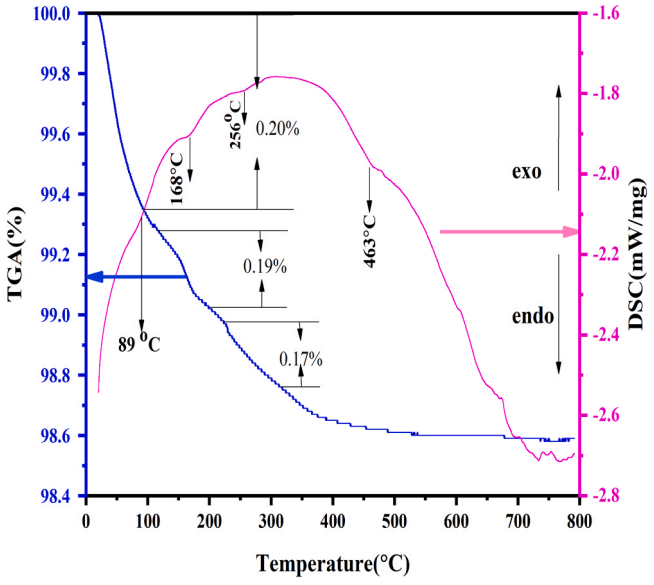

Fig. 6. Combined profiles of TG-DSC profiles of the $BaBPO_5$ phosphor.

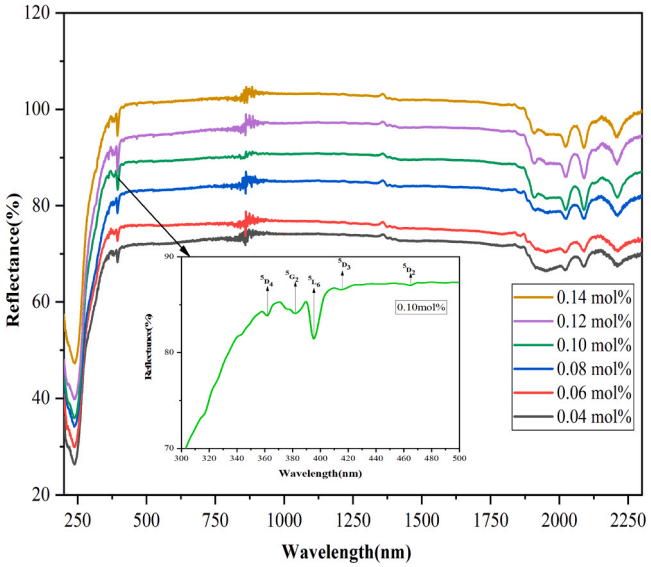

Fig. 7. UV-Visible diffuse reflectance spectra in the range 200 nm - 2300 nm and magnification of 0.1 mol%Eu^{3+} doped $BaBPO_5$ phosphor in the region 300–500 nm.

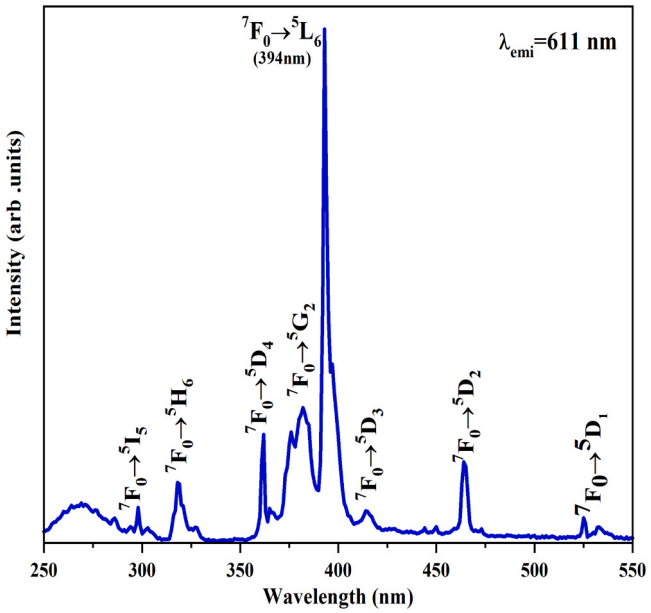

Fig. 8. Excitation (λ_{exi} = 611 nm) spectrum of $BaBPO_5$:0.1 mol% Eu^{3+}.

factor (g) is determined by the ratio of integrated intensity of PSB and of the pure electronic transition (PET) by utilising Eq.6 [52,53].

$$g = \frac{\int I_{PSB}(\lambda)d\lambda}{\int I_{PEB}(\lambda)d\lambda} \quad (6)$$

the above parameter is calculated as 0.12 and 0.08 for PSB1 and PSB2 of $BaBPO_5$:0.1Eu^{3+} phosphor. These values are useful in calculating multiphonon relaxation rates between the excited level to the next lower level.

3.6.2. Multiphonon relaxation rate

The multiphonon relaxation rates can be calculated by using Miyakawa and Dexter theory and is given by the following Eq.7 [50–52].

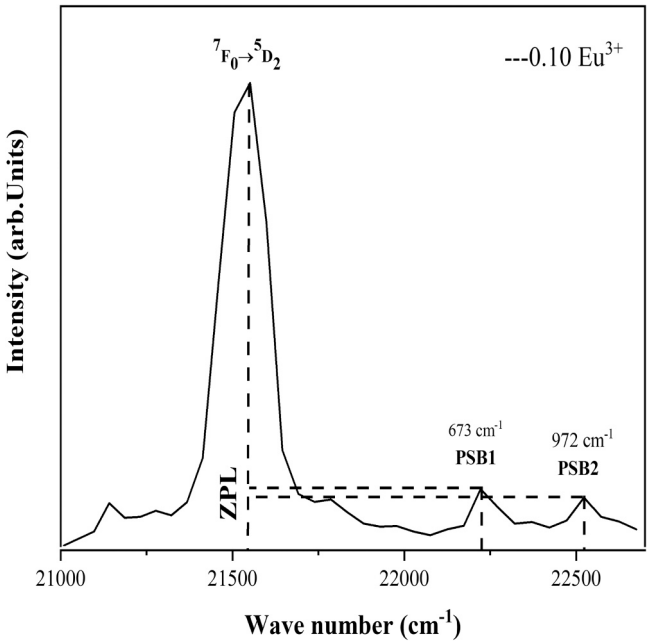

Fig. 9. Phonon side band spectrum of $BaBPO_5$:0.1Eu^{3+} phosphor with $^7F_0 \rightarrow {}^5D_2$ excited state transition.

$$Wmpr = W0\ e^{-\alpha \Delta E} \tag{7}$$

where W_0 is the rate of decay at zero energy gap and zero phonon emission, ΔE is the energy gap of the subsequent levels, α is the host dependent parameter and is provided by Eq.8 [53]:

$$\alpha = (\hbar\omega) - 1 \left[\ln\left(\frac{P}{g_{(n+1)}}\right) - 1\right] \tag{8}$$

where p is the number of phonons needed to bridge the energy gap (ΔE), and n is the partition distribution function for the phonon population, which can be calculated from Eqs.9 and 10 [53]:

$$p = \frac{\Delta E}{\hbar\omega} \tag{9}$$

$$n = \left(e^{\hbar\omega/kT} - 1\right)^{-1} \tag{10}$$

where kT = 208.5 cm^{-1} at room temperature, ħω is the energy of phonon and k is the Boltzmann constant.

In the present phosphor, the energy gaps (ΔE) between the $^5D_1$, $^5D_2$ and $^5D_3$ levels and the subsequent lower level are estimated as 1746 cm^{-1}, 2472 cm^{-1} and 2594 cm^{-1} respectively. The phonon energies of $BaBPO_5$:0.1Eu^{3+} phosphor are 673 cm^{-1} and 972 cm^{-1}. From these values, W_{mpr}/W_0 are determined for $^5D_1$, $^5D_2$ and $^5D_3$ levels and are presented in Table 3. It is noticed that the multiphonon relaxation rate decreases with increase in energy gap (ΔE) and the higher number of phonons (p). The calculated g value is higher in PSB1 than PSB2. The greater value of g is an indication of increasing covalency and strong covalent bonding with the local site. The values of α and W_{mpr}/W_0 are calculated for all transitions and are mentioned in Table 3. These values show a general tendency as $^7F_0 \rightarrow {}^5D_1 > {}^7F_0 \rightarrow {}^5D_2 > {}^7F0 \rightarrow {}^5D_3$ for the transitions in compliance with the theoretical predictions. Lower phonon energies, lower vibrational state energies reduce the nonradiative relaxation rates which can maximize the emission probability [54,55].

Table 3
Host dependent parameter (α), Electron-phonon coupling strengths (g), phonon energies (ħω) and multi-phonon relaxation rates (W_{mpr}/W_0) of $BaBPO_5$:0.1Eu^{3+} phosphor for different transitions of Eu^{3+} ions.

sample	g	ħω (cm^{-1})	$^7F_0 \rightarrow {}^5D_1$		$^7F_0 \rightarrow {}^5D_2$		$^7F_0 \rightarrow {}^5D_3$	
			α ($x10^{-3}$ cm)	W_{mpr}/W_0 ($x10^{-5}$)	α ($x10^{-3}$cm)	W_{mpr}/W_0 ($x10^{-5}$)	α ($x10^{-3}$ cm)	W_{mpr}/W_0 ($x10^{-5}$)
$BaBPO_5$: 0.1Eu^{3+}	0.12	673	3.01	513	3.53	15	3.59	8.8
	0.08	972	2.14	375	2.51	196	2.57	124

3.6.3. Emission spectra

Fig. 10 displays the emission spectra of Eu^{3+} doped $BaBPO_5$ phosphor for different concentrations. The emission spectra were obtained in the range 550–750 nm at $\lambda_{exi} = 394$ nm. It is clear from the emission spectra that it consists of multiple band emissions due to Eu^{3+} ions. The emission spectra with $\lambda_{exi} = 394$ nm shows six peaks at 592 nm, 611 nm, 651 nm, 682 nm - 724 nm corresponding to the transitions $^5D_0 \rightarrow {}^7F_1$, $^5D_0 \rightarrow {}^7F_2$, $^5D_0 \rightarrow {}^7F_3$, and $^5D_0 \rightarrow {}^7F_4$ respectively. Among all the transitions, $^5D_0 \rightarrow {}^7F_1$ and $^5D_0 \rightarrow {}^7F_2$ are more intense observed at 592 nm and 611 nm respectively. These two transitions give orange and red emission. The same is confirmed with the CIE diagram. The luminescence intensities of phosphors are very responsive to symmetry surrounding Eu^{3+} ions [30]. The surrounding ligands of the host material have a small effect on the fluorescence spectrum of Eu^{3+} ion [56].

The transition $^5D_0 \rightarrow {}^7F_1$ is magnetic dipole allowed transition and $^5D_0 \rightarrow {}^7F_2$ is electric dipole allowed transition. Due to the both magnetic dipole and electric dipole transitions, this phosphor exhibits orange-red colour emission. The magnetic dipole transition is allowed according to Judd-Oflet theory. The intensity of magnetic dipole transition ($^5D_0 \rightarrow {}^7F_1$) is not affected by the host lattice environment, but the intensity of electric dipole transition ($^5D_0 \rightarrow {}^7F_2$) depends on the host lattice environment [31]. However, it should be noted that this intensity pertains to the transition's total integrated intensity, not to the intensities of its constituent crystal field components. Overall, the high intensity of $^5D_0 \rightarrow {}^7F_1$ transition in $BaBPO_5$ can be attributed to a combination of factors such as host lattice effects, charge compensation mechanisms, energy transfer process, site symmetry and the quality of the host matrix [24]. The selection rule for $^5D_0 \rightarrow {}^7F_1$ transition is $\Delta J = \pm 1$ [19]. The intensity of the forced electric dipole transition $^5D_0 \rightarrow {}^7F_2$ is very sensitive to the site symmetry or local symmetry of the Eu^{3+} ions. The transition is a so-called "hypersensitive transition". The selection rule for the transition $^5D_0 \rightarrow {}^7F_2$ is $\Delta J = \pm 2$. It is evident from the emission spectra that $^5D_0 \rightarrow {}^7F_2$ is comparatively weaker than $^5D_0 \rightarrow {}^7F_1$, indicating that orange colour emission dominates the luminescence spectrum [30]. The Judd-Ofelt theory states that the transition $^5D_0 \rightarrow {}^7F_3$ is forbidden transition and generally weak. It intensifies only in the presence of substantial crystal field perturbation and strong J-mixing. The addition of Ba^{2+} ions can change the local crystal field around the activator ions, structural changes in the crystal lattice, energy transfer efficiency with in the material, charge compensation mechanisms in the host lattice and can reduce non-radiative relaxations by decreasing phonon energy [57,58]. In the present work, the presence of Ba^{2+} ions induce lattice distortion, resulting in a modification of the crystal field environment around the Eu^{3+} ions and causing a splitting of the energy levels of the Eu^{3+} ions. The division of the energy levels of Eu^{3+} can result in widening of the emission peak $^5D_0 \rightarrow {}^7F_2$. Overall, the photoluminescence of Eu^{3+} is strongly influenced by Ba^{2+} ions [59–62].

Introduction of Eu^{3+} ions into $BaBPO_5$ creates a charge imbalance in the crystal lattice, because Eu^{3+} ions have a different charge compared to Ba^{2+} ions. To maintain charge neutrality, charge compensation mechanism may occur by the creation of oxygen vacancies in the host lattice structure. These vacancies act as charge compensators to balance the charge introduced by the Eu^{3+} ions. The charge compensation can influence the emission spectrum of Eu^{3+} in $BaBPO_5$ phosphor by affecting the crystal field, energy transfer process, quenching effects, and local structural distortions.

The term asymmetry ratio(R_{21}) refers to the ratio of intensities of electric dipole transitions (ED) to magnetic dipole transition (MD) ($^5D_0 \rightarrow {}^7F_2$ / $^5D_0 \rightarrow {}^7F_1$). This asymmetric ratio is given as [56,63,64]:

$$R_{21} = I\ (^5D_0 \rightarrow {}^7F_2) \,/\, I\ (^5D_0 \rightarrow {}^7F_1) \tag{11}$$

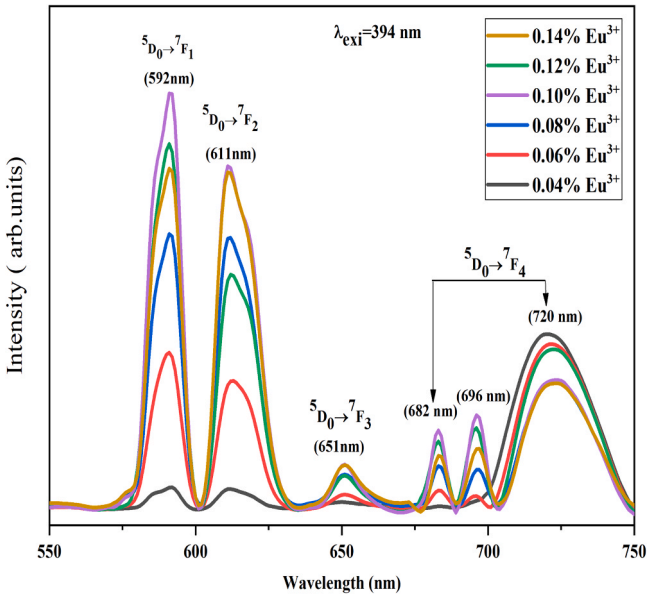

Fig. 10. Emission spectra (λ_{emi} = 394 nm) of $BaBPO_5$: xEu^{3+} (x=0.04, 0.06, 0.08, 0.10, 0.12 and 0.14 mol%) phosphor for different Eu^{3+} concentrations.

This asymmetry ratio provides the information about local symmetry of Eu^{3+} ion and degree of covalency with the ligand anions. In the current phosphor, R_{21} values are 1.16, 1.04, 1.22, 0.82, 1.04, and 1.21 for 0.04, 0.06, 0.08, 0.10, 0.12, and 0.14 mol% of Eu^{3+} ion concentrations, respectively. The higher (R>1) and lower (R<1) values of R_{21} shows asymmetric site and symmetric site around the activator ions, respectively [7]. When the concentration of Eu^{3+} ions in a host material is varied, several factors can affect the R_{21} ratio such as concentration quenching, site occupation, and energy transfer process. For 0.1 mol% of Eu^{3+} ions, the R_{21} value is less than 1, which indicates the occupation of symmetric site by Eu^{3+} in the obtained ligand [60]. The occupation of Eu^{3+} ions in symmetric sites within in a ligand environment can indeed increase luminescence intensity. This enhancement is primarily due to reduced non-radiative decay, effective energy transfer, enhanced electronic transitions, and minimized crystal field splitting. All these factors can lead to sharper emission lines and higher emission intensity. In the present phosphor depicted in Fig. 10, it is evident that the emission peak is more intense when the concentration of Eu^{3+} ions is 0.1 mol% [61]. The transition, $^5D_0 \rightarrow {}^7F_4$ is due to forced electric dipole transition. It is weak in our present phosphor. This is caused due to the replacement of less electro negative Ba^{2+} ions by Eu^{3+} ions and creation of more polarized chemical environment which decreases the local symmetry.

In the present work from Fig. 10, it is clear that the emission intensity increased from 0.04 to 0.10 mol% of Eu^{3+} ion concentrations and decreased at 0.12 mol%, 0.14 mol%, it may be due to concentration quenching. As Eu^{3+} ions concentration increases the distance between ions decreases, due to this a loss of energy transfer and a decrease in luminescence intensity occur [64]. Concentration quenching in the present $BaBPO_5:Eu^{3+}$ phosphor can be ascribed to two distinct mechanisms i.e.,1) cross-relaxation and 2) multi-phonon relaxation. The photoluminescence quenching in cross-relaxation is due to high dopant concentration. In multiphonon relaxation, the host lattice phonon side band spectrum determines the energy transfer that occurs during quenching, which is caused by Eu^{3+} ions and host lattice vibrations [7].

3.7. Energy transfer mechanism

The effective energy transfer mechanism, which has been widely used to study the specific mechanism of the photoluminescence quenching process, is determined by calculating the critical distance (R_c). R_c can be calculated for the present phosphor by using the following Blasse equation [65]:

$$Rc = 2\left(\frac{3V}{4\pi XcN}\right)^{\frac{1}{3}} \tag{12}$$

where X_c is the critical concentration of Eu^{3+} ions, V is the volume of single unit cell and N is the number of unit crystal cells in the formula. Energy transfer takes place by the exchange interaction if the $R_C < 5\ A^0$ and by the multi-polar interaction if $R_C > 5\ A^0$. In present phosphor, the mean critical distance is roughly 10.67 A^0. Hence, multi-polar interaction is responsible for the energy transfer in the present phosphor [30].

According to Dexter theory, the multipolar interaction type can be estimated using the formula [49].

$$\frac{I}{x} = \frac{k}{1+\beta(x)^{\frac{\theta}{3}}} \tag{13}$$

where the parameters for the host are β, k, and x is concentration of Eu^{3+} ion. The above equation can be written as

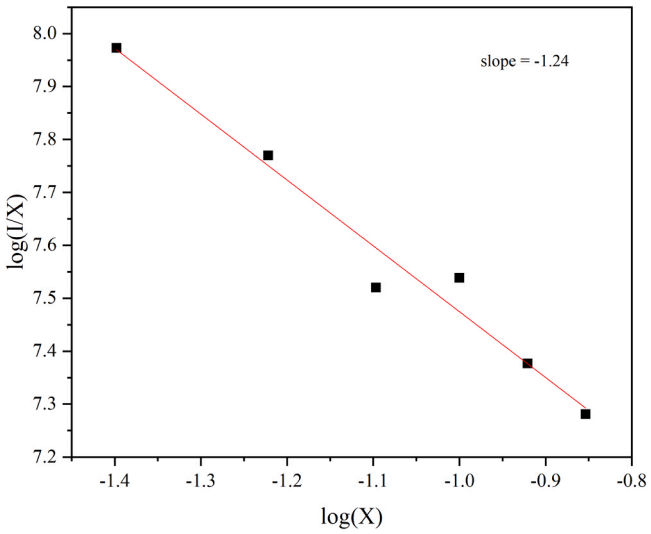

Fig. 11. Variation of log (I/X) with log X in $BaBPO_5$: Eu^{3+} phosphor.

$$\log\left(\frac{I}{x}\right) = C - \frac{\theta}{3}\log(x) \tag{14}$$

where C is the host-related constant. The slope of Eq. (14) yields the value of θ. In this case, the slope of the straight line derived from the plot between log(I/x) and log(x) is used to approximate θ. Fig. 11 shows the variation of log(I/x) with log (x), the graph is linear and its slope is −1.24 and θ value from Eq. (13) is 3.72. For the nearest neighbour ions, the values of the multipolar interaction constant (θ) are 3, 6, 8, or 10, which corresponds to the interactions between dipoles (d-d), quadrupoles (d-q), and quadrupoles (q-q), respectively. In the present phosphor the concentration quenching is due to non-radiative energy transfer at the nearest-neighbour ions [24,55].

3.7.1. Quantum yield

The quantum yield is a measure of how efficiently absorbed energy is converted into emitted light by a phosphor material. In the present work, the internal quantum efficiency (η_{IQE}) of the representative sample $BaBPO_5$: $0.1Eu^{3+}$ phosphor was measured at room temperature using the integrated sphere method as illustrated in Fig. 12. η_{IQE} is calculated by utilising the formula from the reference [65]. The quantum efficiency of above phosphor is 23.86 % indicating lower quantum efficiency which may be due to higher optical band gap and nonradiative relaxation [66]. Fig. 13 shows the partial energy level diagram of excitation and emission bands of $BaBPO_5$: Eu^{3+}.

3.8. Lifetime decay curve analysis

The fluorescent decay lifetime curves of $^5D_0$ level of Eu^{3+} ions in $BaBPO_5$ phosphor are shown in Fig. 14 which are recorded at λ_{exc} = 611 nm and λ_{emi} = 394 nm. A bi-exponential function is fitted to the decay curves. The following equation describes the bi-exponential behaviour [34]:

$$I(t) = I(0) + A_1 \exp(-t/\tau_1) + A_2 \exp(-t/\tau_2) \tag{15}$$

where I(0) is intensity of emission at t=0 ns, I(t) is the intensity at t = t ns, τ_1 and τ_2 are fluorescent decay lifetimes, A_1 and A_2 are the amplitudes of decay. The mean lifetime will be calculated by using

$$\tau\text{mean} = \frac{A_1\tau_1^2 + A_2\tau_2^2}{A_1\tau_1 + A_2\tau_2} \tag{16}$$

The existence of rare earth ions in various contexts within the host matrix and energy transfer between ions, which results in concentration quenching behaviour, are attributed to the bi-exponential behaviour of lifetime [67]. The mean lifetime values of $^5D_0$ level of Eu^{3+} in $BaBPO_5$ phosphor for different concentrations of Eu^{3+} ions are presented in Table 4. In the present phosphor the mean lifetime values are very short. The short lifetime is good for solid state lightning and display technology [24]. The average lifetime values of RE^{3+}ions are typically influenced by defects, the chemical-physical environment, and nonradiative energy transfer. The calculated mean lifetime values of $^5D_0$ level of Eu^{3+} is influenced by multiphonon emission and phonon assisted energy transfer [55, 68].

3.9. Chromaticity co-ordinates

The Commission international de I'Eclairage (CIE) 1931 color coordinates can be used to accurately predict the color emitted by the prepared phosphor using the emission spectra [69]. Fig. 15 shows the chromaticity diagram of $BaBPO_5$: Eu^{3+} phosphor. From the diagram it is observed that the color coordinates represent the reddish orange region of the chromaticity diagram. The colour co-ordinates are calculated by using the formulae [13] as follows:

$$x = \frac{X}{X+Y+Z} \text{and} y = \frac{Y}{X+Y+Z} \tag{17}$$

The calculated color coordinates are presented in Table 5 and it is observed that the coordinates are shifting towards reddish orange region as the concentration of Eu^{3+} ions increased from 0.04 mol% to 0.14 mol%. Under the excitation of 392 nm the present phosphor $BaBPO_5$: Eu^{3+} has coordinates (0.523,0.376), (0.553,0.371), (0.531,0.370) for 0.1, 0.12 and 0.14 mol% respectively. The data indicates that the reddish-orange zone contains the CIE coordinates of the current phosphor. $BaBPO_5$:$0.1Eu^{3+}$ phosphor can be a potential candidate for orange-red emitting phosphor used as a red component of n-UV w-LEDs [70–72]. Co-ordinate color temperature (CCT) is another important parameter to recognize the visual color aspect of the source. The equation given by Mc-Camy is usually used to estimate white light quality according to CCT value(kelvin) as follows [72].

$$CCT = -449\,n^3 + 3525\,n^2 - 6823.3\,n + 5520.33 \tag{18}$$

Warm white light has a CCT value of about 3700 K, while cool white light has a value of about 5000 K. Cool white light is not advised for indoor use due to its high CCT values. Warm white light bulbs are safe and highly recommended for interior residential applications because of their low CCT values, which are advantageous to human eyes. By observing Table 5, the present phosphor is having low CCT values and it is highly suitable for production of warm white LEDs [24]. Color purity of Eu^{3+} ions of different concentrations are calculated using the formula given below [73]:

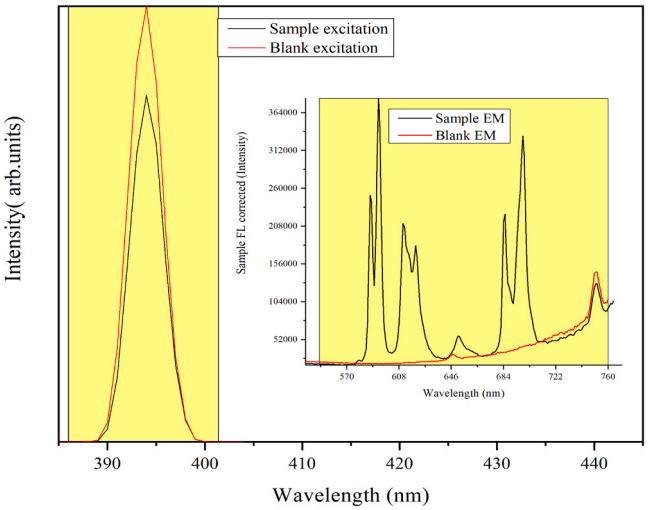

Fig. 12. Quantum efficiency measurement of $BaBPO_5$:0.1Eu^{3+}phosphor made using integrating sphere.

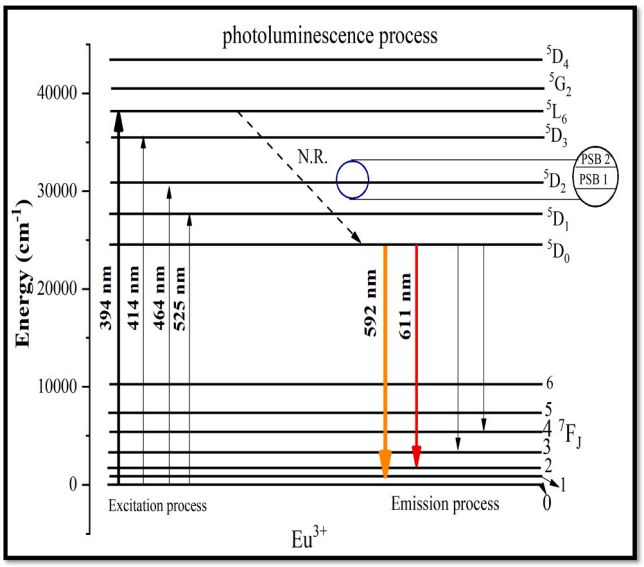

Fig. 13. Partial energy level diagram of Eu^{3+} doped $BaBPO_5$ phosphor showing excitation and emission.

$$\text{color purity} = \frac{\sqrt{(x-x_i)^2+(y-y_i)^2}}{\sqrt{(x_d-x_i)^2+(y_d-y_i)^2}}\text{x}100 \tag{19}$$

The phosphor's color purity at a given concentration is denoted in the equation above by (x, y). The white source's color coordinate has a value of (0.33, 0.33) and is represented by (xi, yi). (x_d, y_d) is the predominant wavelength of color coordinate. The color purities of $BaBPO_5$: xEu^{3+} phosphor for x = 0.04, 0.06, 0.08, 0.1, 0.12 and 0.14 mol% are obtained as 20, 48, 73, 84, 83 and 76 % respectively. By looking at the above data, $BaBPO_5$:0.1Eu^{3+} phosphor exhibits a sharper color purity compared to the other concentrations of Eu^{3+} ions. This makes this phosphor a great choice for warm White-LED applications [40,74,75].

4. Conclusions

The $BaBPO_5$: Eu^{3+} phosphors were synthesized via solid state reaction technique. Properties such as structural, morphological, elemental, thermal and photoluminescence were studied. The crystallinity nature of $BaBPO_5$: Eu^{3+} phosphor was examined using XRD examinations, and its structure was found to be trigonal (hexagonal axis) crystal structure with COD Entry no: 96–151–1443. From the crystal size calculation, it was observed that the crystal size is smaller in Debye-Scherrer's method as compared to William-Hall method

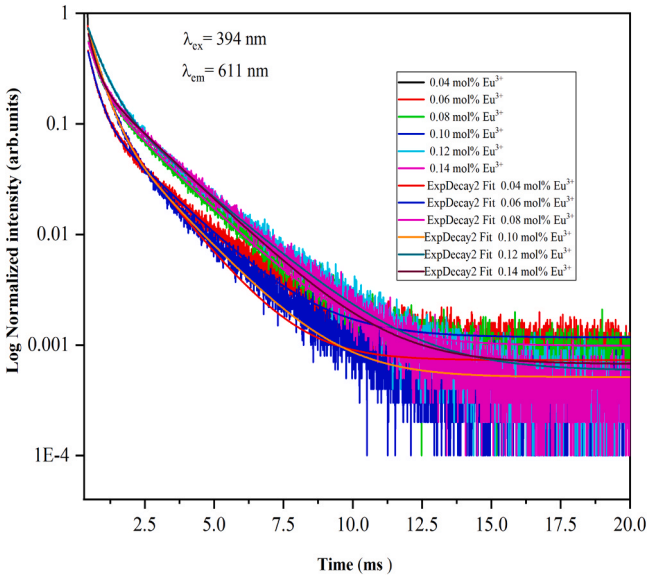

Fig. 14. Life time decay curves of $^5D_0$ level of Eu^{3+} doped $BaBPO_5$ phosphor.

Table 4
Mean lifetime values (τ_{mean}) of $^5D_0$ level of $BaBPO_5$: Eu^{3+} for different concentrations of Eu^{3+} ions.

S.No	Concentration(x) mol%	Lifetime ($\tau_{mean)\ ms}$	χ^2
1	0.04	0.685	0.98
2	0.06	1.245	0.99
3	0.08	1.093	0.99
4	0.10	0.728	0.99
5	0.12	1.395	0.99
6	0.14	1.469	0.99

due to lattice strain consideration. According to the FTIR spectral analysis, the $BaBPO_5$:Eu^{3+} phosphor's highest phonon energy was measured at 1196 cm^{-1}. The FE-SEM image analysis showed irregular particles for the prepared $BaBPO_5$: 0.1 %Eu^{3+} phosphor, which is a suitable host in phosphate family. TGA analysis indicated that the phosphor is highly stable at higher temperatures and from DSC curve three endothermic peaks were identified. The highest band gap was observed for $BaBPO_5$: 0.04 %Eu^{3+} and values are slightly decreasing with increase in Eu^{3+} concentration. The higher band gap values indicated that it is suitable for optoelectronic applications. The PL excitation spectra exhibited the strongest absorption peak centred at 394 nm, suggested that this phosphor can be efficaciously excited by the n-UV light. Phonon energies, electron-phonon coupling strengths and multiphonon relaxation rates were calculated from phonon side band spectrum of the $BaBPO_5$: Eu^{3+}. The two phonon energies associated with the ZPL are found to be 673 cm^{-1}, 972 cm^{-1} which are in agreement with vibrational modes. Multiphonon relaxation rates were calculated for PSB1 and PSB2. The PL spectra show multiple peaks due the transitions, $^5D_0 \rightarrow {}^7F_J$ ($J = 0, 1, 2, 3, 4$) of Eu^{3+} ions. Concentration quenching was happened in the $BaBPO_5$: Eu^{3+} phosphors when the doping concentration of Eu^{3+} exceeds 0.1 mol%. The mean critical distance (R_c) of Eu^{3+} in $BaBPO_5$: Eu^{3+} phosphors was found to be approximately 10.67 A°, and neighbouring ions accounted for majority of the energy transfer between Eu^{3+} ions. So, the optimum concentration for efficient luminescence is $BaBPO_5$: $0.1Eu^{3+}$. The quantum efficiency of $BaBPO_5$:$0.1Eu^{3+}$ phosphor was 23.86 %. The CIE chromaticity coordinates of $BaBPO_5$:0.1 Eu^{3+} phosphor was obtained as (0.553, 0.371) position in the reddish-orange region. Thus Eu^{3+} doped $BaBPO_5$ reddish-orange emitting phosphor is promising to be a potential candidate for widely used n-UV pumped w-LEDs.

Author agreement statement

We the undersigned declare that this manuscript entitled "**Novel reddish-orange emitting $BaBPO_5$:Eu^{3+} phosphor for n-UV warm white-LEDs: synthesis and study of structural and spectroscopic investigations**" is original, has not been published before and is not currently being considered for publication elsewhere. We confirm that the manuscript has been read and approved by all named authors and that there are no other persons who satisfied the criteria for authorship but are not listed. We further confirm that the order of authors listed in the manuscript has been approved by all of us.We understand that the Corresponding Author is the sole contact for the Editorial process. He is responsible for communicating with the other authors about progress, submissions of revisions and final approval of proofs.

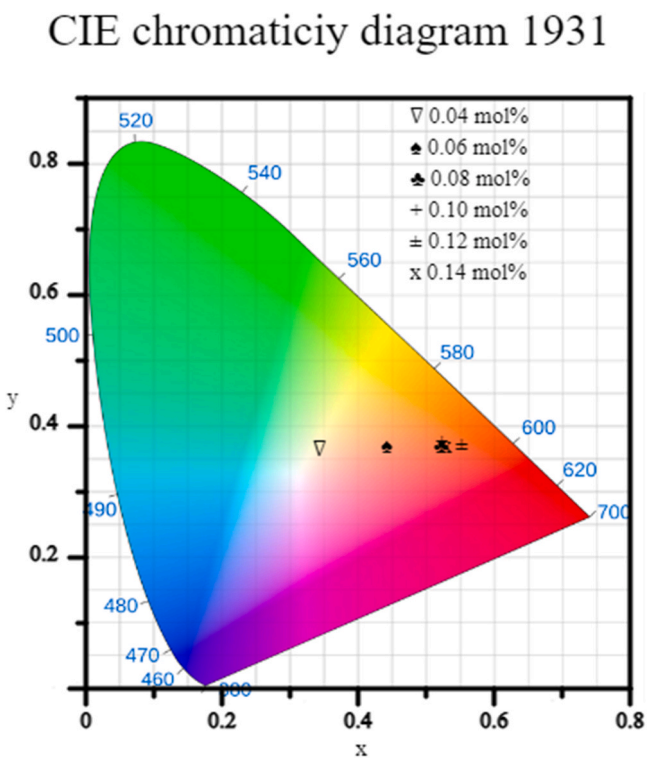

Fig. 15. The CIE 1931 chromaticity co-ordinate diagram for $BaBPO_5:Eu^{3+}$ phosphor under 394 nm excitation.

Table 5
CIE color coordinates and CCT values of $BaBPO_5$: Eu^{3+} phosphor for different concentrations of Eu^{3+} ions.

S. No	Concentration (x) mol%	CIE color coordinates		CCT (K)
		X	Y	
1	0.04	0.343	0.364	5095
2	0.06	0.443	0.368	2573
3	0.08	0.520	0.368	1792
4	0.10	0.553	0.371	1812
5	0.12	0.523	0.376	1714
6	0.14	0.531	0.370	1755

CRediT authorship contribution statement

P. Sai Dinesh: Data curation. **K. Venkata Rao:** Visualization. **Y.C. Ratnakaram:** Supervision, Conceptualization. **T. Raghu Raman:** Resources, Formal analysis. **T Chandra Mohan:** Writing – original draft.

Declaration of Competing Interest

The authors declare that, they have no known competing financial interests or personal relationships that could have appeared to influence the work reported in this paper. We have authority over manuscript preparation and decisions to submit the manuscript for publication

Acknowledgements

One of the authors, T. Chandra Mohan, expresses his sincere thanks to SAIF MGU, Kottayam, VIT Vellore, SAIF IIT Madras, and SAIF IIT BOMBAY for providing characterization facilities.

Data Availability

Data will be made available on request.

References

[1] C.H. Huang, C.T. Chen, S. Guo, J.Y. Zhang, W.R. Liu, Luminescence and theoretical calculations of novel red-emitting $NaYPO_4F:Eu^{3+}$ phosphor for LED applications, J. Alloy. Compd. 712 (2017) 225–232.
[2] X. Huang, "Solid-state lighting: Red phosphor converts white LEDs, Nat. Photonics 8 (2014) 748–749.
[3] J. Liang, B. Devakumar, L. Sun, S. Wang, Q. Sun, X. Huang, Full-visible-spectrum lighting enabled by an excellent cyan-emitting garnet phosphor, J. Mater. Chem. C 8 (14) (2020) 4934–4943.
[4] X. Huang, J. Liang, S. Rtimi, B. Devakumar, Z. Zhang, Ultra-high color rendering warm-white light-emitting diodes based on an efficient green-emitting garnet phosphor for solid-state lighting, Chem. Eng. J. 405 (2021) 126950.
[5] L. Cao, W. Li, B. Devakumar, N. Ma, X. Huang, A.F. Lee, Full-spectrum white light-emitting diodes enabled by an efficient broadband green-emitting $CaY_2ZrScAl_3O_{12}:Ce^{3+}$garnet phosphor, ACS Appl. Mater. Interfaces 14 (2022) 5643–5652.
[6] J. Chan, L. Cao, Z. Xu, X. Huang, Cation substitution induced highly symmetric crystal structure in cyan-green-emitting Ca_2La_{1-x} $Lu_xHf_2Al_3O_{12}:Ce^{3+}$ solid-solution phosphors with enhanced photoluminescence emission and thermal stability: toward full-visible-spectrum white LEDs", Mater. Today Phys. 35 (2023) 101130.
[7] M.T. Tran, N. Tu, N.V. Quang, D.H. Nguyen, L.T.H. Thu, D.Q. Trung, P.T. Huy, Excellent thermal stability and high quantum efficiency orange-red-emitting $AlPO_4:Eu^{3+}$ phosphors for WLED application, J. Alloys Compd. 853 (2021) 156941.
[8] H. Guo, L. Sun, J. Liang, B. Li, X. Huang, High-efficiency and thermal-stable Eu^{3+}-activated $Ca_3Y(AlO)_3(BO_3)_4$ red-emitting phosphors for near-UV-excited white LEDs, ", J. Lumin 205 (2019) 115–121.
[9] J. Zhu, M. Yang, Y. Che, Z. Fang, Y. Zheng, D. Yang, Y. Mao, K. Xiong, J. Liao, Europium (III) doped $LiNa_2B_5P_2O_{14}$ phosphor: Surface analysis, DFT calculations and luminescent properties", J. Alloys compd. 822 (2020) 153606.
[10] S.V.G.V.A. Prasad, G. Sahaya Baskaran, N. Veeraiah, Spectroscopic, magnetic and dielectric investigations of $BaO-Ga_2O_3-P_2O_5$ glasses doped by Cu ions, Phys. Status Solidi (A) Appl. Mater. Sci. 202 (2005) 2812–2828.
[11] M. Dhavamurthy, P. Vinothkumar, A. Antony Suresh, M. Mohapatra, P. Murugasen, Optical characteristics of Eu^{3+} doped alumino borophosphate glass containing Al^{3+}, Zn^{2+}, Li^{2+}, Sr^{2+} and Ba^{2+} ions, Results Opt. 8 (2022) 100232.
[12] K. Laxminarayana, K. Srikanth, M. Narsimulu, L. Narsihma, M. Satish Kumar, M. Srinivas, Luminescence studies of europium and terbium doped calcium orthosilicate phosphors, Mater. Today Proc. 59 (2022) 742–746.
[13] V. Reddy Prasad, B. Haritha, S. Damodaraiah, Y.C. Ratnakaram, Influence of Nd^{3+} and Er^{3+} concentration on NIR luminescence properties in calcium borophosphate (CBP) phosphors, Infrared Phys. Technol. 94 (2018) 184–190.
[14] X. Huang, Z. Xu, B. Devakumar, Near-UV-excitable broadband green-emitting $Ca_2LaHf_2GaAl_2O_{12}:Ce^{3+}$ garnet-type phosphors for high color rendering warm-white LEDs", Ceram. Int 49 (2023) 26420–26427.
[15] N. Ma, W. Li, B. Devakumar, X. Huang, Dazzling red-emitting europium(III) ion-doped $Ca_2LaHf_2Al_3O_{12}$ garnet-type phosphor materials with potential application in solid-state white lighting, Inorg. Chem. 61 (2022) 6898–6909.
[16] N. Ma, W. Li, B. Devakumar, Z. Zhang, X. Huang, Utilizing energy transfer strategy to produce efficient green luminescence in $Ca_2LuHf_2Al_3O_{12}:Ce^{3+}$, Tb^{3+} garnet phosphors for high-quality near-UV-pumped warm-white LEDs, J. Colloid Interface Sci. 601 (2021) 365–377.
[17] Z.M. Wang, R.M. Osgood, J. Parisi, Springer Series in Materials Science Volume 174 Series Editors, n.d.
[18] A. George, A. Jose, T. Krishnapriya, P.R. Biju, Synthesis and spectroscopic characterization of $Ba_2Sb_2O_7:Eu^{3+}$ orange-red emitting phosphor for WLEDs, Mater. Lett. 300 (2021).
[19] M. Rajendran, S. Vaidyanathan, High performance red/deep-red emitting phosphors for white LEDs, New J. Chem. 44 (2020) 5354–5365.
[20] M. Wu, B. Chen, C. He, X. Huang, Q. Liu, X. Min, R. Mi, X. Wu, M. Fang, Y. Liu, Z. Huang, A high quantum yield red phosphor $NaGdSiO_4$: Eu^{3+} with intense emissions from the $^5D_0 \rightarrow {}^7F_{1,2}$ transition", Ceram. Int 48 (2022) 23213–23223.
[21] A. Balakrishna, L. Reddy, O.M. Ntwaeaborwa, H.C. Swart, Remarkable influence of alkaline earth ions on the enhancement of fluorescence from Eu^{3+} ion doped in sodium ortho-phosphate phosphors, J. Mol. Struct. 1203 (2020) 127375.
[22] D. Chitnis, N.T. Kalyani, S.J. Dhoble, Portrayal of structural, thermal and optical properties of pH sensitive Eu (TTA)3bipy hybrid organic complex for OLEDs, Optik 130 (2017) 237–244.
[23] T. Raghu Raman, B.D. Raju, Y.C. Ratnakaram, Photoluminescence investigations of Eu^{3+}-doped $LiPbB_5O_9$ as a red emitting phosphor for warm W-LED applications, Indian J. Phys. 96 (2022) 1547–1558.
[24] K. Binnemans, Interpretation of europium (III) spectra, Coord. Chem. Rev. 295 (2015).
[25] R. Cao, X. Lv, Y. Jiao, Y. Ran, S. Guo, H. Ao, T. Chen, T. Fan, $Ca_3La_6Si_6O_{24}:Eu^{3+}$ orange-red-emitting phosphor: Synthesis, structure and luminescence properties, Mater. Res Bull. 122 (2020).
[26] G. Annadurai, B. Li, B. Devakumar, H. Guo, L. Sun, X. Huang, Synthesis, structural and photoluminescence properties of novel orange-red emitting $Ba_3Y_2B_6O_{15}$: Eu^{3+} phosphors, ", J. Lumin 208 (2019) 75–81.
[27] C. Ji, Z. Huang, X. Tian, W. Xie, J. Wen, H. He, C. Zhou, T. Zeng, Synthesis and photoluminescence properties of a novel $BaGe_4O_9:Eu^{3+}$ red emitting phosphor for warm white LEDs", Dyes Pigments 160 (2019) 772–778.
[28] M. Rajendran, S. Vaidyanathan, New red emitting phosphors $NaSrLa(MO_4)_3:Eu^{3+}$ [M = Mo and W] for white LEDs: synthesis, structural and optical study, J. Alloy. Compd. 789 (2019) 919–931.
[29] S. Wang, Y. Xu, T. Chen, W. Jiang, J. Liu, X. Zhang, W. Jiang, L. Wang, A novel red phosphor $Ba_2La_4Y_4(SiO_4)_6O_2$: Eu^{3+} with high quantum yield and thermal stability for warm white LEDs", J. Alloy. Compd. 789 (2019) 381–391.
[30] G. Yuan, R. Cui, J. Zhang, X. Zhang, X. Qi, C. Deng, Photoluminescence evolution and high thermal stability of orange red-emitting $Ba_{3-x}Sr_xZnNb_2O_9$: Eu^{3+} phosphors, J. Solid State Chem. 303 (2021).
[31] J. Xiang, J. Zheng, Z. Zhou, H. Suo, X. Zhao, X. Zhou, N. Zhang, M.S. Molokeev, C. Guo, Enhancement of red emission and site analysis in Eu^{2+} doped new-type structure $Ba_3CaK(PO_4)_3$ for plant growth white LEDs, Chem. Eng. J. 356 (2019) 236–244.
[32] Dy Pushcharovsky, E. Gobetchia, M. Pasero, S. Merlino, O.V. Dimitrova, "Hydrothermal synthesis and crystal structures of $LiBaB_9O_{15}$, and $BaBPO_5$", 2002.
[33] Y. Shi, J. Liang, H. Zhang, Q. Liu, X. Chen, J. Yang, W. Zhuang, G. Rao, "Crystal Structure and Thermal Decomposition Studies of Barium Borophosphate, $BaBPO_5$", 1998.
[34] T.R. Raman, Y.C. Ratnakaram, Concentration dependent Dy^{3+} activated $LiPbB_5O_9$ phosphor: Structure and luminescence studies for white LED applications, Opt. Mater. (Amst.) 99 (2020).
[35] T. Krishnapriya, A. Jose, T.A. Jose, A.C. Saritha, C. Joseph, P.R. Biju, Investigation of the structural and photoluminescence properties of Eu^{3+} doped $Na_6CaP_2O_9$ phosphors for solid state lighting, Mater. Res Bull. 139 (2021).
[36] M. Pal, U. Pal, J. Miguel, G.Y. Jiménez, F. Pérez-Rodríguez, "Effects of crystallization and dopant concentration on the emission behavior of TiO_2: Eu nanophosphors", 2012.
[37] T. Raghu Raman, Y.C. Ratnakaram, B. Deva Prasad Raju, Synthesis and spectroscopic investigations on Pr_{3+}-doped $LiPbB_5O_9$ phosphor: a blue converting red phosphor for white LEDs, Optik 225 (2021).
[38] P.V. Campos, A.R.L. Albuquerque, R.S. Angélica, S.P.A. Paz, FTIR spectral signatures of amazon inorganic phosphates: igneous, weathering, and biogenetic origin, Spectrochim. Acta A Mol. Biomol. Spectrosc. 251 (2021).
[39] Y.A. Yamusa, R. Hussin, W.N. Wan Shamsuri, S.A. Dalhatu, A.M. Aliyu, I. Bulus, Structural, optical and physical properties of Dy_{3+} ions in barium sulphate borophosphate glasses for generation of white light, Int J. Mod. Phys. B 32 (2018).
[40] T.R. Raman, V.R. Prasad, A.V. Reddy, Y.C. Ratnakaram, Photoluminescence properties of Sm_{3+} -doped $LiPbB_5O_9$ phosphor for reddish-orange emitting light applications, ", J. Lumin 217 (2020).

[41] V. Reddy Prasad, S. Damodaraiah, S.N. Devara, Y.C. Ratnakaram, Photoluminescence studies on holmium (III) and praseodymium (III) doped calcium borophosphate (CBP) phosphors, J. Mol. Struct. 1160 (2018) 383–392.

[42] H. Takebe, T. Harada, M. Kuwabara, Effect of B_2O_3 addition on the thermal properties and density of barium phosphate glasses, J. Non Cryst. Solids 352 (2006) 709–713.

[43] Y. Zhao, Y. Zhou, J. Yang, Y. Li, L. Cheng, K. Wang, X. Sun, C. Sun, Z. Qin, Optimized structural and mechanical properties of borophosphate glass, Ceram. Int 46 (2020) 9025–9029.

[44] P. Kalenda, L. Koudelka, P. Mošner, L. Beneš, Thermal behavior and the properties of $BaO–B_2O_3–P_2O_5$ glasses, J. Therm. Anal. Calor. 124 (2016) 1161–1168.

[45] P. Makuła, M. Pacia, W. Macyk, How to correctly determine the band gap energy of modified semiconductor photocatalysts based on UV-Vis spectra, J. Phys. Chem. Lett. 9 (2018) 6814–6817.

[46] V.B. Pawade, A. Zanwar, R.P. Birmod, S.J. Dhoble, L.F. Koao, Optical and bandgap study of rare earth doped phosphate phosphor, J. Mater. Sci. ", Mater. Electron. 28 (2017) 16306–16313.

[47] T. Munawar, M.S. Nadeem, F. Mukhtar, M. Hasan, K. Mahmood, M.I. Arshad, A. Hussain, A. Ali, M.S. Saif, F. Iqbal, Rare earth metal co-doped $Zn_{0.9}La_{0.05}M_{0.05}O$ (M = Yb, Sm, Nd) nanocrystals; energy gap tailoring, structural, photocatalytic and antibacterial studies, Mater. Sci. Semicond. Process 122 (2021).

[48] C. Liu, Z. Zhou, Y. Zhang, Synthesis and luminescence properties of novel red-emitting $Na_2ZnSiO_4:Eu^{3+}$ phosphor with intense $^5D_0 \rightarrow {}^7F_4$ transition and high quantum yield", J. Alloy. Compd. 787 (2019) 1158–1162.

[49] G.Kaur Behrh, R. Gautier, C. Latouche, S. Jobic, H. Serier-Brault, Synthesis and photoluminescence properties of $Ca_2Ga_2SiO_7:Eu^{3+}$ red phosphors with an intense $^5D_0 \rightarrow {}^7F_4$ transition", Inorg. Chem. 55 (2016) 9144–9146.

[50] R. Skaudzius, A. Katelnikovas, D. Enseling, A. Kareiva, T. Jüstel, Dependence of the $^5D_0 \rightarrow {}^7F_4$ transitions of Eu^{3+} on the local environment in phosphates and garnets, ", J. Lumin 147 (2014) 290–294.

[51] N.T.Q. Lien, H.Van Tuyen, N.H. Vi, A.N.H. Thuan, P.Van Do, Site occupancy and phonon sideband of trivalent europium doped calcium aluminosilicate phosphors, Opt. (Stuttg.) 241 (2021).

[52] M. Wachtler, A. Speghini, S. Pigorini, R. Rolli, M. Bettinelli, Phonon sidebands and vibrational properties of Eu^{3+} doped lead germanate glasses, Lett. Ed. (1997).

[53] D. Ramachari, L. Rama Moorthy, C.K. Jayasankar, Phonon sideband spectrum and vibrational analysis of Eu^{3+}-doped niobium oxyfluorosilicate glass, J. Lumin 143 (2013) 674–679.

[54] A. Jose, P. Remya Mohan, T. Krishnapriya, T.A. Jose, A.C. Saritha, N.V. Unnikrishnan, C. Joseph, P.R. Biju, Phonon sideband and Judd–Ofelt analyses of trivalent europium doped fluoroborosilicate glasses for red emitting device applications, J. Mater. Sci. Mater. Electron. 31 (2020) 13531–13540.

[55] P. Manasa, C.K. Jayasankar, Luminescence and phonon side band analysis of Eu^{3+}-doped lead fluorosilicate glasses, Opt. Mater. (Amst.) 62 (2016) 139–145.

[56] S. Karthika, M.S. Sajna, S. Thomas, K.P. Revathy, P.R. Biju, N.V. Unnikrishnan, Structural and optical studies of Eu^{3+}/nanocrystallites doped titania-zirconia hybrids", J. Alloy. Compd. 615 (2014) 188–193.

[57] R. Okram, N.R. Singh, 2013, Photoluminescence Behaviours of CePO4: Tb3+, M (M = Li+, Ba2+, Bi3+) Nanoparticles Synthesized in Different Reaction Medium..

[58] H. Zhang, D. Yuan, X. Mi, X. Liu, J. Lin, Color tuning in $Ca_{3-x}Mx(PO_4)_2:Eu^{2+}$(M = Sr, Ba) phosphors via cation substitution, Dalton Trans. 49 (2020) 8949–8958.

[59] R. Vijayakumar, B. Devakumar, G. Annadurai, H. Guo, X. Huang, Novel high color purity and thermally stable Eu^{3+} ions activated $Ba_2Gd_5B_5O_{17}$ red emitting phosphor for near-UV based WLEDs, Opt. Mater. (Amst.) 84 (2018) 312–317.

60] T. Zhao, N. Chen, G. Du, C. Jiang, Effect of Ba^{2+} doping on the photoluminescence of YVO4: Eu^{3+} phosphor and first principles calculations, J. Lumin 222 (2020).

[61] Y. Shuanglong, C. Xianlin, Z. Chaofeng, Y. Yunxia, C. Guorong, Eu^{2+}, Mn^{2+} Co-doped (Sr, Ba)$_6BP_5O_{20}$ - A novel phosphor for white-LED, Opt. Mater. (Amst.) 30 (2007) 192–194.

[62] R. Singh, A. King, B.B. Nayak, Influence of dopant concentration on powder morphology and photoluminescence characteristics of red-emitting Eu^{3+}-doped ZnO, Opt. (Stuttg.) 247 (2021).

[63] H. Duan, R. Cui, J. Li, C. Deng, Synthesis and photoluminescence properties of a novel red emitting $Ba_3ZnTa_2O_9$: Eu^{3+} phosphor, J. Mol. Struct. 1224 (2021).

[64] R.A. Sá Ferreira, S.S. Nobre, C.M. Granadeiro, H.I.S. Nogueira, L.D. Carlos, O.L. Malta, A theoretical interpretation of the abnormal $^5D_0 \rightarrow {}^7F_4$ intensity based on the Eu^{3+} local coordination in the $Na_9[EuW_{10}O_{36}] \cdot 14H_2O$ polyoxometalate", J Lumin 121 (2006) 561–567.

[65] X. Ouyang, R. Liu, X. Hu, J. Li, R. Tang, X. Jin, S. Chen, X. Yao, B. Deng, H. Geng, R. Yu, Preparation, characterization, and application of a red phosphor $Ca_2InTaO_6:Eu^{3+}$ in w-LEDs and latent fingerprint detection, J. Alloy. Compd. 939 (2023).

[66] T. Krishnapriya, A. Jose, T.A. Jose, A.C. Saritha, C. Joseph, P.R. Biju, Investigation of the structural and photoluminescence properties of Eu^{3+} doped $Na_6CaP_2O_9$ phosphors for solid state lighting, Mater. Res Bull. 139 (2021).

[67] Y. Chen, Q. Guo, L. Liao, M. He, T. Zhou, L. Mei, M. Runowski, B. Ma, Preparation, crystal structure and luminescence properties of a novel single-phase red emitting phosphor $CaSr_2$ $(PO_4)_2$: Sm^{3+},Li^{+}", RSC Adv. 9 (2019) 4834–4842.

[68] T.R. Raman, R.P. Vijaya lakshmi, Y.C. Ratnakaram, Effect of Ho^{3+} ion concentration on structure and spectroscopic properties of $LiPbB_5O_9:Ho^{3+}$ phosphor, J. Mol. Struct. 1243 (2021).

[69] S.C. Lal, J. Isuhak Naseemabeevi, S. Ganesanpotti, Distortion induced structural characteristics of $Ba_2R_{2/3}TeO_6$(R = Y, Gd, Tb, Dy, Ho, Er, Tm, Yb and Lu) double perovskites and their multifunctional optical properties for lighting and ratiometric temperature sensing, Mater. Adv. 2 (2021) 1328–1342.

[70] E.F. Huerta, O. Soriano-Romero, A.N. Meza-Rocha, S. Bordignon, A. Speghini, U. Caldiño, Lithium-aluminum-zinc phosphate glasses activated with Sm^{3+}, Sm^{3+}/Eu^{3+} and Sm^{3+}/Tb^{3+} for reddish-orange and white light generation, J. Alloy. Compd. 846 (2020).

[71] J. Du, D. Xu, X. Gao, Z. Yang, J. Sun, A novel orange-red emitting phosphor Sr_3Lu $(PO_4)_3$: Sm^{3+} for near UV-pumped white light-emitting diodes, J. Mater. Sci. Mater. Electron. 28 (2017) 8136–8143.

[72] Q. Wu, Y. Xie, F. She, Q. Zhao, J. Ding, J. Zhou, $CsBaB_3O_6$: Eu^{3+} red-emitting phosphors for white LED and FED: crystal structure, electronic structure and luminescent properties, J. Rare Earths 39 (2021) 1040–1048.

[73] S. Wang, X. Qiao, Synthesis and photoluminescence properties of novel orange-red emitting triphosphate $CaNa_4(P_3O_9)_2$: Eu^{3+} phosphor, Opt. Mater. 98 (2019).

[74] L.L. Devi, C.K. Jayasankar, Novel reddish-orange color emitting $Ca_2SiO_4:Sm^{3+}$ phosphors for white LED applications prepared by using agricultural waste, J. Lumin 221 (2020).

[75] M. Derbel, A. Mbarek, G. Chadeyron, Novel reddish-orange emitting ultraphosphate $CaP_4O_{11}:Eu^{3+}$ phosphor: synthesis and photoluminescence properties, J. Photochem. Photobio. A Chem. 409 (2021).